ADVANCED ENERGY MATERIALS
www.advenergymat.de

Cooling Induced Surface Reconstruction during Synthesis of High-Ni Layered Oxides

Ming-Jian Zhang, Xiaobing Hu, Maofan Li, Yandong Duan, Luyi Yang, Chong Yin, Mingyuan Ge, Xianghui Xiao, Wah-Keat Lee, Jun Young Peter Ko, Khalil Amine, Zonghai Chen, Yimei Zhu, Eric Dooryhee, Jianming Bai, Feng Pan,* and Feng Wang**

Transition metal layered oxides have been the dominant cathodes in lithium-ion batteries, and among them, high-Ni ones ($LiNi_xMn_yCo_zO_2$; $x \geq 0.7$) with greatly boosted capacity and reduced cost are of particular interest for large-scale applications. The high Ni loading, on the other hand, raises the critical issues of surface instability and poor rate performance. The rational design of synthesis leading to layered $LiNi_{0.7}Mn_{0.15}Co_{0.15}O_2$ with greatly enhanced rate capability is demonstrated, by implementing a quenching process alternative to the general slow cooling. In situ synchrotron X-ray diffraction, coupled with surface analysis, is applied to studies of the synthesis process, revealing cooling-induced surface reconstruction involving Li_2CO_3 accumulation, formation of a Li-deficient layer and Ni reduction at the particle surface. The reconstruction process occurs predominantly at high temperatures (above 350 °C) and is highly cooling-rate dependent, implying that surface reconstruction can be suppressed through synthetic control, i.e., quenching to improve the surface stability and rate performance of the synthesized materials. These findings may provide guidance to rational synthesis of high-Ni cathode materials.

Li-ion batteries (LIBs) are now increasingly used in electric vehicles (EVs) and other large-scale applications, but a bottleneck for their mass adoption is low Li-storage capacity, which is largely constrained by cathodes, typically with a gravimetric capacity equivalent to ≈1/2 that of the graphite anode. Despite much research into candidate cathodes for LIBs, transition metal (TM) layered oxides with a hexagonal structure (space group $R\bar{3}m$) have remained dominant over the past three decades.[1,2] In particular, high-Ni layered oxides, $LiNi_xMn_yCo_zO_2$ (NMC; $x \geq 0.7$) are now attracting world-wide interest for their high theoretical capacity (≈280 mA h g^{-1}), which, however, has been difficult to realize due to the issues associated with high Ni loading:[3–8] in addition to cationic disordering (Li/Ni mixing) and the resulted low electrochemical activity,[9–11]

Dr. M.-J. Zhang, M. Li, Dr. Y. Duan, Dr. L. Yang, Prof. F. Pan
School of Advanced Materials
Peking University
Shenzhen Graduate School
Shenzhen 518055, P. R. China
E-mail: panfeng@pkusz.edu.cn

Dr. M.-J. Zhang, Dr. Y. Duan, C. Yin, Dr. F. Wang
Sustainable Energy Technologies Department
Brookhaven National Laboratory
Upton, NY 11973, USA
E-mail: fwang@bnl.gov

Dr. X. Hu, Dr. Y. Zhu
Condensed Matter Physics and Materials Science Department
Brookhaven National Laboratory
Upton, NY 11973, USA

Dr. Y. Duan
School of Science
Hebei University of Science and Technology
Shijiazhuang 050018, P. R. China

C. Yin
Ningbo Institute of Materials Technology and Engineering
Chinese Academy of Sciences
Ningbo 315201, P. R. China

Dr. M. Ge, Dr. X. Xiao, Dr. W.-K. Lee, Dr. E. Dooryhee, Dr. J. Bai
National Synchrotron Light Source II
Brookhaven National Laboratory
Upton, NY 11973, USA
E-mail: jmbai@bnl.gov

Dr. J. Y. P. Ko
The Cornell High Energy Synchrotron Source
Cornell University
Ithaca, NY 14853, USA

Dr. K. Amine, Dr. Z. Chen
Electrochemical Technology Program
Chemical Sciences and Engineering Division
Argonne National Laboratory
9700 South Cass Avenue, Lemont, IL 60439, USA

Dr. K. Amine
Materials Science and Engineering
Stanford University
Stanford, CA 94305, USA

Dr. K. Amine
Institute for Research and Medical Consultations (IRMC)
Imam Abdulrahman Bin Faisal University (IAU)
Dammam 34212, Saudi Arabia

The ORCID identification number(s) for the author(s) of this article can be found under https://doi.org/10.1002/aenm.201901915.

DOI: 10.1002/aenm.201901915

cycling stability and safety are often compromised due to the surface-related issues.[12–15]

Significant efforts in developing high-Ni NMC cathodes have been put on studying electrochemical impact, origin of the Li/Ni disordering, and on improving Li/Ni ordering through optimizing synthesis conditions.[9,11,16,17] It is until very recently that people started to pay close attention to the surface instability, particularly surface reconstruction, including formation of NiO-type rock salt,[11,18,19] Li_2CO_3 species,[10,14,20–22] and nickel carbonate ($NiCO_3 \cdot 2Ni(OH)_2 \cdot 2H_2O$).[23] These surface species are electrochemically inactive and poor in electronic and ionic conductivity, so causing high impedance to Li^+ (de)intercalation during cycling,[24,25] and even power fade as reported in $LiNi_{0.8}Co_{0.2}O_2$.[26] The formation of NiO and Li_2CO_3 at the surface of primary particles may also accelerate cracking in the secondary particles, eventually leading to the capacity fade with cycling.[27] Surface Li_2CO_3 was recently shown to be the main source of CO_2 and CO generated during the first charge, and it reacts with electrolyte to produce LiF and gases, consequently causing impedance increase, capacity and power fade.[28,29] To alleviate those issues associated with these detrimental surface species, post-synthesis processing procedures, such as washing, surface coating, are mostly taken, but they also cause reduced capacity and cost increase.[22,30,31]

Recent studies demonstrate that stoichiometric high-Ni NMC oxides with high structural ordering may be obtained through rational design of synthesis devised to control the cationic ordering as the materials are synthesized,[9,11] but the surface reconstruction, shown as Ni reduction and off-stoichiometry at the particle surface (i.e., Li-deficiency), was found to be an issue.[11] Such surface construction was observed ex situ, on the samples cooled down to room temperature, and it is still unclear how the surface reconstruction happens during synthesis. In the studies of solid-state synthesis of Li-rich layered oxides, experimental evidences were provided to show the impact of the cooling process on their structural ordering and electrochemical properties.[32–35] But so far, there has been no report on studies of the cooling process in Li-rich or Ni-rich layered oxides, e.g., how the structure, both in the bulk and surface at the particle surface, evolves in the materials upon cooling (as the final step of synthesis).

In this work, by taking $LiNi_{0.7}Mn_{0.15}Co_{0.15}O_2$ (NMC71515) as a representative of high-Ni layered oxides, we first investigate how synthesis conditions, particularly the cooling rate, affect the structural evolution, not only in the bulk, but also at the surface. As illustrated in **Scheme 1**a,b, the insulating Li_2CO_3 and NiO-type rock salt, once formed at the surface, would cause impedance to the Li extraction/insertion. Therefore, systemic structural/electrochemical characterization is made to NMC71515 obtained through slow cooling and quenching, using multiple techniques, X-ray photoelectron spectroscopy (XPS), transmission X-ray microscopy (TXM), scanning transmission electron microscopy-electron energy loss spectroscopy (STEM-EELS), and electrochemical impedance spectroscopy (EIS). In order to understand how the surface reconstruction occurs, the whole synthesis process is tracked in situ using temperature-resolved synchrotron X-ray diffraction (XRD) technique, which captures all of the crystalline species, not only the main layered phases, but those formed at the surface, such as Li_2CO_3 (as in Scheme 1c).

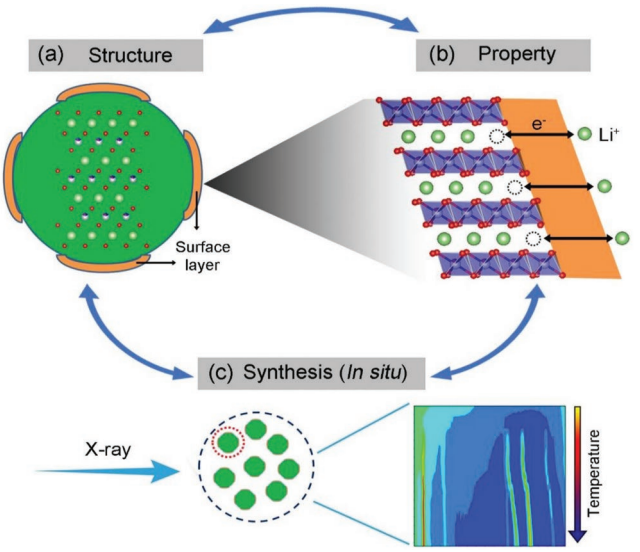

Scheme 1. Schematic illustration of the approach with a "closed" loop for rational design of synthesis in making high-Ni layered oxides, specifically, through studying the surface reconstruction and its impact to electrochemical properties, and its formation process (via in situ X-ray study). a,b) Formation of a surface layer, and the potential impact on the electrochemical performance due to impedance to the Li extraction/insertion during charging/discharging. c) In situ X-ray studies of the synthesis process using temperature-resolved synchrotron X-ray diffraction technique that has high enough detection efficiency to track the formation of Li_2CO_3 (despite its weak scattering of X-ray; inset).

Through this study, we reveal, for the 1st time, the cooling-induced surface reconstruction during synthesis of NMC71515, leading to buildup of surface Li_2CO_3, formation of a Li-deficient layer and Ni reduction at the particle surface. Such surface reconstruction that occurs mainly at high temperatures (above 350 °C), is different than that during storage or electrochemical cycling. In addition, we demonstrated that, the kinetic reconstruction process is cooling rate dependent, and can be suppressed by quenching, to improve rate performance. Findings from this study, particularly the origin of surface reconstruction, and the demonstrated solutions to alleviate the issue, may inspire new strategies for synthetic design of high-Ni layered oxide cathodes.

In order to study the impact of cooling process on the structural properties of NMC71515, two type of samples were prepared by slow cooling (cooling rate: 2 °C min^{-1}) and quenching (cooling rate: 200 °C min^{-1}), respectively. Structure analysis of the two samples was made by synchrotron XRD, showing no obvious difference as shown in **Figure 1**a. Rietveld refinements were performed, with the main results provided in Figure 1b and Figure S1 and Table S1 (Supporting Information). Ni occupancy at 3b site (Ni(3b)) for the sample obtained by slow cooling is 0.017, about 0.010 less than that for the sample obtained by quenching (0.027). In addition, the Li-slab distance in the sample by slow cooling is almost the same as that in the sample by quenching (slightly larger; Table S1, Supporting Information). Electrochemical tests were also performed on the samples obtained to evaluate the impact of cooling rate on electrochemical performance. The charging/

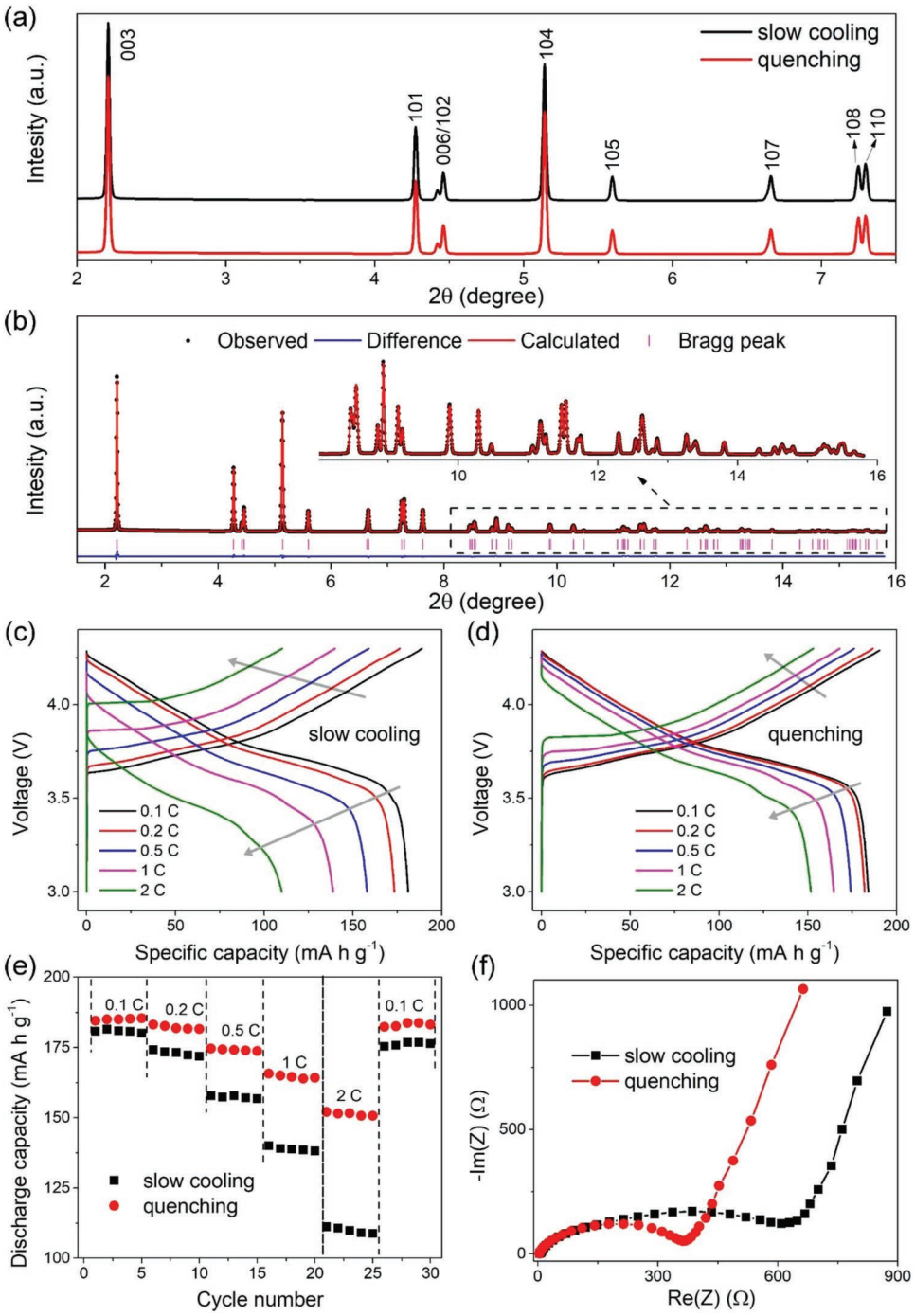

Figure 1. Structural and electrochemical properties of NMC71515 synthesized using same heating procedures but different rates during cooling. a) Synchrotron XRD patterns from the two types of samples via slow cooling and quenching, showing the high similarity of their structure in the bulk. b) Comparison between experimental XRD pattern for the sample obtained by slow cooling and the calculated pattern by Rietveld refinement using a single rhombohedral structure model ($R\bar{3}m$). c,d) Voltage profiles for the 1st charge/discharge at different rates, 0.1, 0.2, 0.5, 1, and 2 C, for the samples obtained by slow cooling and quenching, respectively, showing much reduced polarization in the latter case. e) Discharge capacities in the potential range of 3.0–4.3 V (vs Li^+/Li) at different rates, 0.1, 0.2, 0.5, 1, and 2 C, showing the much higher rate capability of the sample by quenching. f) Nyquist plots of the impedance, showing the much reduced charge transfer resistance of the sample by quenching (red), about ½ that of the sample by slow cooling (black).

discharging profiles at different rates, as given in Figure 1c,d, clearly show the much larger increase of the electrochemical polarization in the sample by slow cooling, especially at the high rates; correspondingly, show the specific capacity is much lower, compared to the sample by quenching, which is further demonstrated by the rate performance as provided in Figure 1e.

When the rate increases from 0.1 to 0.2, 0.5, 1, and 2 C, the discharge capacity in the sample obtained by quenching is slowly reduced, by 1.7%, 5.9%, 11.1%, and 18.1%, respectively, relative to the capacity at 0.1 C; such a rate performance is much better than the previous report on the samples by the natural cooling.[36] In contrast, the capacity of the sample by slow cooling is significantly reduced (by 4.3%, 12.8%, 23.3%, and 39.3%). In addition, during elongated cycling process higher capacity was achieved in the sample by quenching (Figure S2, Supporting Information). Since the particle sizes of both samples are nearly the same (Figure S3, Supporting Information), the superior performance of the sample by quenching could be ascribed to the lower impedance, as shown in Figure 1f. For better understanding of their electrochemical behaviors, local structural/chemical analysis at the particle surface was further made.

A combination of surface-sensitive XPS and local probing techniques including TXM, STEM-EELS, was applied to examine the local surface chemistry of the samples obtained by slow cooling and quenching. In the XPS spectra for O 1s as shown in **Figure 2**a, there are two main peaks that are well separated from each other: the left one is ascribed to the O atoms of metal carbonate, namely Li_2CO_3, and the right one comes from the O atoms of metal oxides, namely layered oxides (being illustrated by the fitting). Therefore, the relative content of Li_2CO_3 at the particle surface can be quantified by the ratio between the integrated areas of these two fitted peaks (denoted as $I_{Carbonate}/I_{Oxide}$), as given in Figure 2b. Clearly, the $I_{Carbonate}/I_{Oxide}$ value for the sample obtained by quenching is strikingly smaller, by around 50%, than that for the sample obtained by slow cooling.

The Ni, Co, and Mn 2p XPS spectra were also recorded to check the valence states of the TM cations (Figure S4, Supporting Information). The same position (779.7 eV) of the Co $2p_{3/2}$ peaks indicates Co(III) at the particle surface in both samples. Similar with Co, there is only Mn $2p_{3/2}$ peak associated with Mn(IV) in both samples (at 641.8 eV). In contrast, two separated peaks are seen in Ni $2p_{3/2}$, due to the presence of reduced Ni, i.e., Ni(II), in addition to Ni(III) at the particle surface. To quantify their relative concentration, peak fitting was performed to the two separated peaks associated with Ni(III) and Ni(II), as depicted by magenta and olive colors, respectively (Figure 2c).[24,37,38] As shown in Figure 2d, the ratios between the integrated areas of the two peaks, $I_{Ni(III)}/I_{Ni(II)}$, for two samples are both lower than that in the bulk (3.67, calculated by the nominal composition), which indicates less Ni(III) contents at the surface than that in the bulk for two samples. It can be interpreted by the reduction from Ni(III) to Ni(II) at the surface.

To further determine the local variation in the valence state of Ni across secondary particles, 2D valence map was performed on both NMC71515 samples using TXM-X-ray absorption near-edge spectroscopy (XANES), a powerful technique for spectro-imaging covering a wide energy range, making it an ideal tool to study the valence distribution in NMC cathodes.[39,40] Figure 2e and Figure S5 (Supporting Information) show the 2D valence maps of Ni for NMC71515 obtained by slow cooling and quenching. Ni(II) and Ni(III) are uniformly distributed within secondary particles, showing the similar chemical homogeneity with more Ni(III) than Ni(II) for both samples. Through quantitative analysis to the local Ni(II)/Ni(III) distribution (as given in Figure 2e and Figure S5f, Supporting Information), the average ratios of Ni(III)/Ni(II) was estimated be around 4.0 for both samples, which is essentially consistent with the nominal transition metal composition. Due to the insufficient spatial resolution of TXM (≈30 nm), the local Ni(II)/Ni(III) distribution within primary particles, especially at the surface, cannot be resolved. Therefore, spatially resolved EELS were recorded from individual primary particles using a sub-nm STEM probe. Figure 2f presents the high-angle annular dark-field (HAADF) image taken from the near-edge region of one primary particle obtained by slow cooling. Ni $L_{2,3}$ EELS spectra were recorded from 7 areas (marked by 7 spots with different colors) along the arrow shown in HAADF image. From the fine structure and energy position of Ni L_3-edge, which imprint the electronic structure of the sample, we can study the evolution of oxidation states of Ni from the surface to the bulk. As shown in Figure 2f, Ni L_3-edge shifts to higher energies from the surface to the bulk, hinting at an increased oxidation state of Ni.[26,41–43] These results from spatially resolved EELS not only verified the observation by XPS (Figure 2d), but also unambiguously determined localized distribution of the reduced Ni(II), spanning around 20 nm from the surface to the bulk. Similar trends of changes in the Ni oxidation states were also observed in the sample by slow cooling (Figure S6, Supporting Information).

Results from the characterizations above indicate that, the sample obtained by slow cooling has better cationic ordering in the bulk, but more serious surface reconstruction at the surface compared to the sample obtained by quenching. Such surface reconstruction, involving a Li-deficient layer as well as Li_2CO_3 at the surface, is detrimental to the electrochemical performance as reported previously,[28,44–46] and may even become dominant.

To investigate how the cooling rate affects the kinetics of cationic ordering and surface reconstruction in NMC71515 upon cooling, comparative in situ synchrotron XRD study was performed, with the main results provided in **Figure 3** and Figure S7 (Supporting Information). During the measurements, same heating procedures but different cooling procedures, slow cooling and quenching, with rates of 2 and 200 °C/min^{-1}, respectively, were employed (inset in Figure 3a).

Figure 3a shows the temperature-resolved in situ XRD patterns taken during the slow cooling, a process as taken during ex situ experiment (and generally employed in preparing NMC oxides). In addition to the main phase of layered oxides (space group $R\bar{3}m$), a trace amount of Li_2CO_3 (space group $C2/c$) is observed in the low angle region (between 2.4° and 4.1°; as marked by the dashed square). The high cationic ordering of the layered structure at high temperature (850 °C) is confirmed by the stronger peak of 003 compared to 104 and the pronounced peak splitting between 018 and 110.[9,11] Results from temperature-resolved in situ XRD during quenching were provided in Figure S7a (Supporting Information), also showing the formation of the Li_2CO_3 and high cationic ordering. For a better view of the structural evolution, representative 003, 104, and 018/110 peaks associated with the layered phase are plotted in contour mode, provided in Figure S7b–g (Supporting Information) for the samples by quenching and slow cooling, respectively.

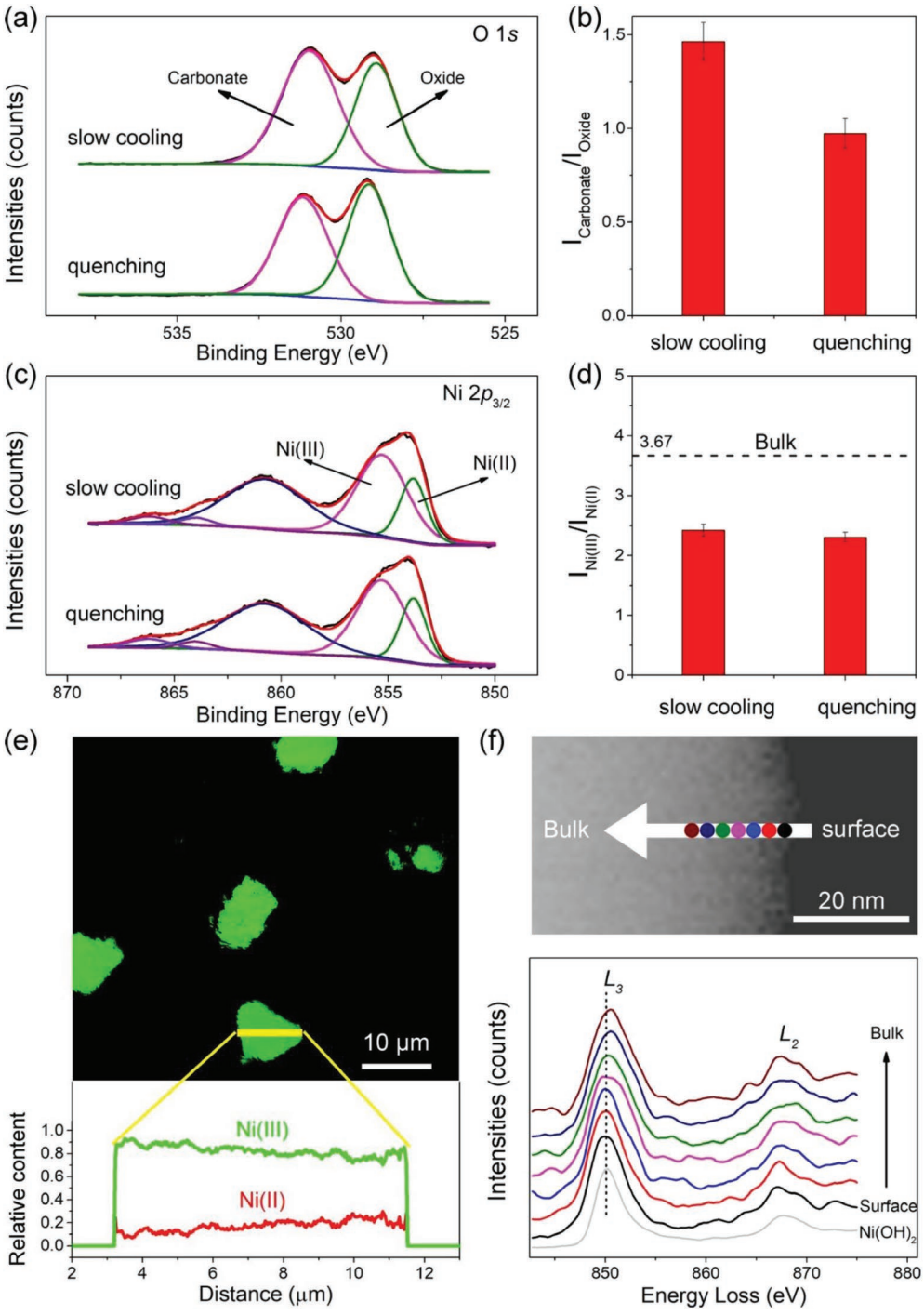

Figure 2. Chemical analysis of surface reconstruction in the synthesized NMC71515. a) The XPS spectra of O 1s for the samples obtained by slow cooling and quenching, respectively. The fitted two peaks come from the signal of the O atoms in carbonates (magenta) and layered oxides (olive), respectively. b) The ratios of the integrated areas of two fitted peaks in (a) (denoted as $I_{Carbonate}/I_{Oxide}$), indicating the relative content of surface Li_2CO_3. c) The Ni 2p XPS spectra for the samples obtained by slow cooling and quenching. 5-peak fitting is performed for both spectra. There into, the peaks in magenta and olive represent Ni(III) and Ni(II), respectively. d) The integrated area ratios of Ni(III) and Ni(II) peaks (denoted as $I_{Ni(III)}/I_{Ni(II)}$) in (c), indicating the average chemical compositions of different Ni valence states at the particle surface. e) TXM-XANES analysis of the Ni chemical state across secondary particles obtained by slow cooling. Top panel: the false colored 2D valence map of Ni(II)/Ni(III) distribution, wherein Ni(II) and Ni(III) are represented by red and green colors, respectively. Bottom: quantitative analysis of Ni(II)/Ni(III) distribution across one single secondary particle (indicated by a yellow line). Ni (II) is hardly observed due to the low concentration, but well resolved in the Ni(II) map as in Figure S5a,c (Supporting Information). f) STEM-EELS analysis of the Ni chemical state at the near-surface region of a single primary particle obtained by slow cooling. Ni $L_{2,3}$-edge EELS spectra were recorded from 7 spots as marked with different colors shown in the high-angle annual dark-field image (HAADF) image (top). Ni $L_{2,3}$-edge spectrum from $Ni(OH)_2$ is presented by the dashed curve as a standard of Ni(II).

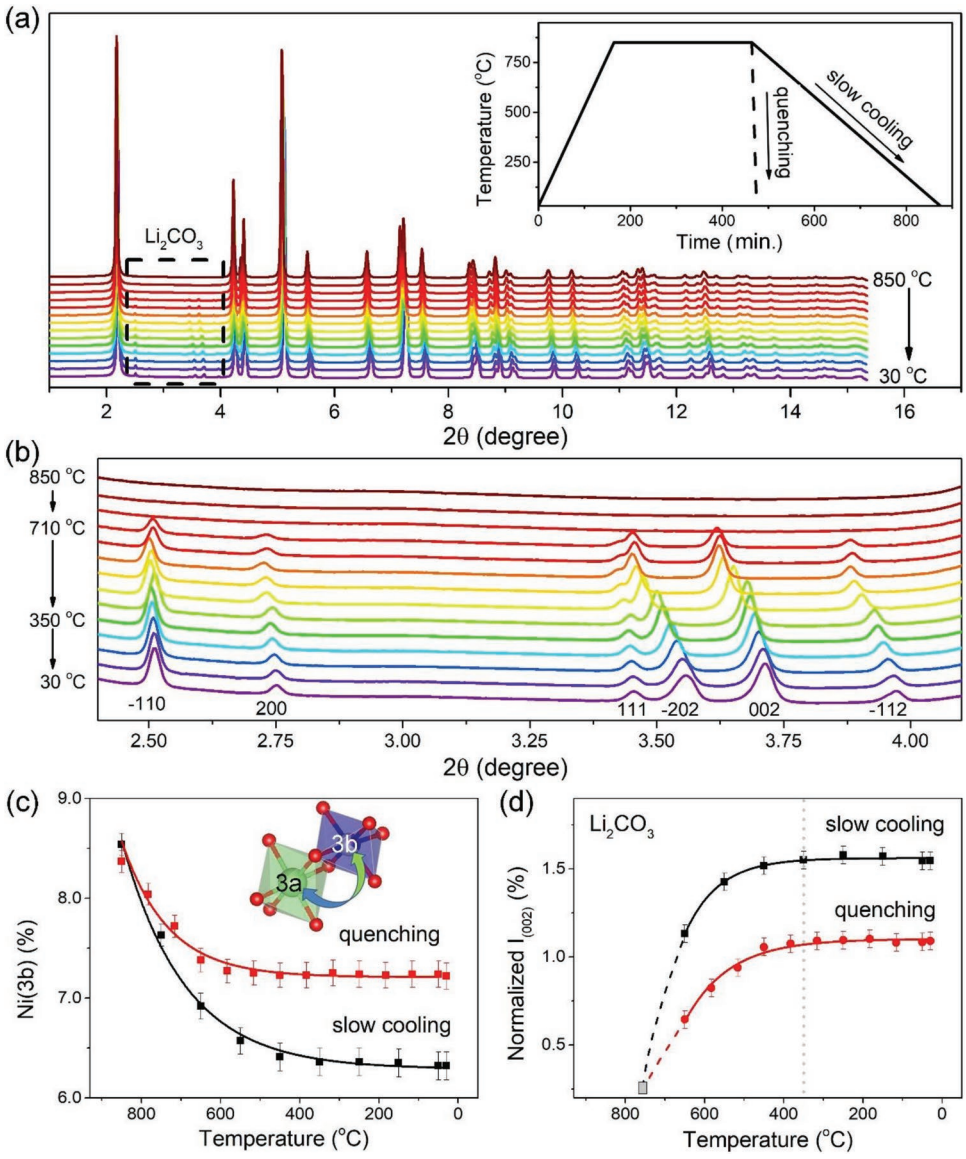

Figure 3. In situ tracking of the structural evolution and formation of Li_2CO_3 in NMC71515 upon cooling during synthesis. a) Temperature-resolved in situ XRD patterns recorded during the slow cooling process (see also Figure S7 (Supporting Information) for the data recorded during quenching); Inset: temperature profiles of in situ experiments with the same temperature-ramping and holding procedures but different cooling procedures, namely slow cooling and quenching (as labeled), using cooling rates of 2 and 200 °C min^{-1}, respectively. b) Zoom-in view of the diffraction patterns associated with the Li_2CO_3 phase, as marked by the black dashed square in (a). c) The evolution of the percentage of Ni at 3b sites, Ni(3b), as a function of temperature; see also Table S2 (Supporting Information) for the results from the Rietveld refinement. The curves are the fitting to the data using an exponential equation $y = Aexp(kT) + y_0$ (wherein A is the pre-exponential factor, and k is the rate coefficient). Inset: schematic illustration of Li/Ni ordering process, showing inter-diffusion of Li/Ni ions between 3a sites (in the TM layers) and 3b sites (in the Li layers). d) The evolution of the integrated area of 002 peak associated with Li_2CO_3 (denoted as $I_{(002)}$, and normalized by $I_{(104)}$ of the layered oxides) as a function of temperature, which are fitted using the exponential equation $y = Aexp(kT) + y_0$ (solid curves). The dashed lines are extended from the fitting lines and crossed at the gray square, indicating the initial formation of Li_2CO_3 at around 750 °C No obvious increase of the peak intensity at temperatures below 350 °C (as marked with a dotted line).

Figure 3b presents the zoom in view of the diffraction peaks associated with Li_2CO_3, showing that they are initially observed at 710 °C (below the melting point, 723 °C). As the temperature continuously decreases, the peaks associated with Li_2CO_3 shift to higher angles, which could be ascribed to the thermal effect, namely lattice contraction as temperature decreases. Moreover, the peak intensities of two characteristic peaks, –110 and 002, increase above 350 °C, which could be attributed to the crystallinity enhancement or a phase concentration increase. The trend of changes can be better seen in the contour map (Figure S8a, Supporting Information). Similar trend is observed during quenching (Figure S8b, Supporting Information), but with a different kinetic process of forming Li_2CO_3, as discussed below through quantitative analysis.

In order to obtain inherent structural changes and the associated kinetics of cationic ordering with temperature in the

layered oxides, quantitative analysis via Rietveld refinement of selected XRD patterns were performed (with all the relevant refinement parameters presented in Figures S9 and S10 and Table S2, Supporting Information). Figure 3c shows the percentage of Ni at Li sites (namely, Ni(3b)) as a function of temperature, an important indicator for Li/Ni ordering.[9] Prior to the cooling process, the Ni(3b) values for both slow cooling and quenching cases are nearly the same, around 8.5%. Upon slow cooling, the Ni(3b) value gradually decreases to about 6.3%. While, the Ni(3b) value for the quenching case drops to 7.2%. The slower cooling rate leads to a higher Li/Ni ordering (by a relative 14%). The results are overall consistent with the ex situ experiments (Table S1, Supporting Information).

For quantitative analysis of the kinetics of forming Li_2CO_3, without the influence of thermal effect and crystallinity improvement, we normalized the integrated area of representative 002 peak for Li_2CO_3 (denoted as normalized $I_{(002)}$) by the integrated area of 104 peak associated with the layered oxides. As shown in Figure 3d, the change of Li_2CO_3 content follows a similar trend for the slow cooling and quenching cases, both fast increasing above 350 °C, then keeping constant, which indicates a thermodynamically favored reaction.[18] Similar to the Li/Ni ordering (Figure 3c), the increase of Li_2CO_3 content is also cooling-rate dependent and, during quenching the speed of forming Li_2CO_3 is much reduced, leading to a smaller amount of Li_2CO_3 in the final product, by 30% than the slow cooling case. Similar results are also obtained from ex situ experiments (Table S1, Supporting Information). The curves for the Li_2CO_3 content in the two cases, once extrapolated to the direction of high temperatures, cross at around 750 °C (marked with a gray square), where Li_2CO_3 is initially formed, basically at a temperature close to its melting point (723 °C).

According to the thermogravimetric analysis (TGA) of Li_2CO_3 during heating at 850 °C, Li_2CO_3 completely decomposes into Li_2O in about 1 h (Figure S11, Supporting Information). In the diffraction data (as in Figure 3a,b), no observation of diffraction peaks associated with Li_2O above 710 °C indicates that, Li source has been mostly exhausted before cooling. Thus those Li for forming Li_2CO_3 should come from the lattice of the layered oxides, and the gradual increase of Li_2CO_3 content indicates the continuous Li loss from the bulk to the surface to react with CO_2 as temperature decreases, which is also supported by the TGA analysis on the weight gains during the cooling process (Figure S12, Supporting Information). During slow cooling, more weight gains are observed at the temperatures above 350 °C, which is consistent with the increase of Li_2CO_3 content (Figure 3d) and may be explained by the continuous production of Li_2CO_3 through adsorbing CO_2 in the air.[18] In contrast, small weight gains are observed during quenching, which is consistent with small Li_2CO_3 content and Li loss from the layered oxides.

The observation of the surface reconstruction, induced by cooling, is different from those reports of surface Li_2CO_3 accumulation in $LiNiO_2$ and high-Ni layered oxides during the storage under ambient conditions.[18,45,47,48] It should be noted that, although Li also comes from the lattice, the observed surface Li_2CO_3 accumulations during storage occurs slowly at room temperature and becomes observable only after elongated time, which, through this study, may be better understood, since Li_2CO_3 content is nearly constant below 350 °C (Figure 3d). Surface reconstruction induced by cooling is much more severe than that during storage, due to the thermal driven solid-gas interaction as discussed immediately below.

The combined in situ and ex situ analysis reveals that, in addition to the cationic ordering in the bulk, surface reconstruction occurs upon cooling, involving Li/O loss from the lattice, arising from solid-gas interaction, as in many other solid-state reactions at elevated temperatures. When subjected to heat treatment at high temperatures (i.e., 850 °C as in this experiment), Li in NMC oxides becomes highly mobile and tends to diffuse out of the lattice. Through optimizing the synthesis conditions (temperature, holding time) in the experiments, well-ordered layered structure was obtained by the end of the holding, both in the bulk and at the surface, with most of Li source being exhausted (as illustrated in **Figure 4**a; left). During the cooling process, especially when the temperature drops below the melting point of Li_2CO_3, no further external Li source is supplied from the surface for compensating Li loss (since all Li are fixed in the solid Li_2CO_3). However, Li keeps migrating out of the lattice in the near-surface region, driven by the Li concentration gradient, so leading to the formation of a Li-deficient layer and build-up of Li_2CO_3 at the surface. Meanwhile, partially reduction of Ni(III) to Ni(II) occurs due to O loss in the Li-deficient layer. (Figure 4a; right).

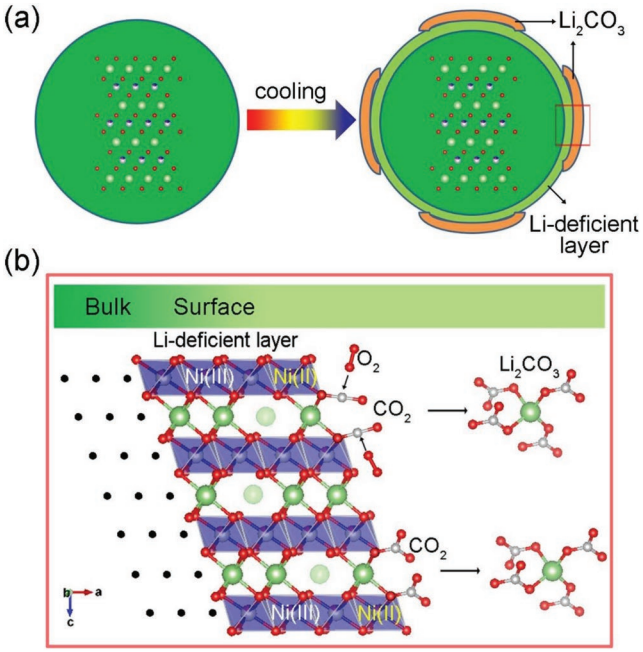

Figure 4. Schematics of cooling-induced surface reconstruction in a primary particle. a) Evolution of a primary particle, from initially optimized cationic ordering in the bulk and clean surface at high temperature, to the particle with surface reconstruction after cooling, involving a Li-deficient layer with partially reduced Ni(III/II) and Li_2CO_3 at the surface. b) Schematic illustration of the surface reconstruction in the near-surface region due to thermal driven solid–gas interaction (mainly with CO_2). The atoms are distinguished using different colors: O - red, C - gray, Li - green, and TM - mixed colors within blue octahedra.

The surface reconstruction is complex in nature especially during high-temperature heat treatment, on one hand due to the intrinsically different structural ordering at the surface compared to that in the bulk, and importantly, thermal driven solid-gas interaction and so dynamic structural evolution involved. In the specific system of metal oxides, the symmetry breaking of MO_6 (M = Li and transition metals) octahedra is expected at the surface, wherein some O vacancies may exist, causing high reactivity at the solid/gas interface. CO_2 molecules in the air could be adsorbed onto the exposed Li^+ ions at the solid/gas interface, through two possible adsorption ways, as illustrated in Figure 4b: 1) O atoms in CO_2 molecules directly coordinate with Li^+ ions due to the nature of Lewis acid, then external O_2 molecules attack the activated C atoms in CO_2; 2) C atoms in CO_2 directly attack the O atoms of LiO_x polyhedral because of the electronegative nature of O atoms. Following these steps, the surficial Li^+ ions will be extracted from layered oxides to form Li_2CO_3. Driven by the Li^+ concentration gradient from the bulk to the surface, Li^+ ions in the bulk (near the surface) could be continuously extracted, at high rate when the temperature is high, and eventually a Li-deficient layer would be formed in the near-surface region. The whole surface reconstruction process could be interpreted by the following reaction, by referring to the previous studies[18]

$$\begin{aligned}&Li_1\left[Ni(III)_{0.55}\,Ni(II)_{0.15}\,Co_{0.15}Mn_{0.15}\right]O_2\,(s)+x/2CO_2\,(g)\rightarrow\\&\quad Li_{1-x}\left[Ni(III)_{0.55-y}\,Ni(II)_{0.15+y}\,Co_{0.15}Mn_{0.15}\right]O_{2-x/2-y/2}\,(s)\\&\quad +x/2Li_2CO_3\,(s)+y/4O_2\,(g)\end{aligned}\qquad(1)$$

Broadly speaking, such a phenomenon observed during cooling may have a common origin as other types of surface reconstruction upon exposed to the air, liquid or other media, all being initialized by the intrinsic symmetry breaking of MO_6 octahedra at the surface. For example, surface reconstruction occurs commonly in electrodes upon exposure to the electrolyte and/or during electrochemical cycling, as in recent studies, and is attributed to the reaction between organic molecules in the electrolyte and partially coordinated metal cations in MO_6 octahedra at the particle surface.[12,13,47,49–52] During storage in the air, $O_2/H_2O/CO_2$ could also react with these partially coordinated metal cations and so surface reconstruction occurs, leading to species like LiOH, Li_2CO_3, and $LiHCO_3$ at the surface.[18,30,45,48,53–57] Such surface reconstruction during storage is found to be Ni content dependent, and more serious in high-Ni NMC cathodes, as a result of high reactivity of Ni(III) at the surface.[58] The consequence of surface reconstruction during storage/cycling is similar to that induced by cooling, but it should also be noted that the cooling induced surface reconstruction is more serious, especially at the high temperatures (above 350 °C), as demonstrated in this study (Figure 3d).

As demonstrated above, surface reconstruction has big impact on electrochemical performance, due to formation of Li_2CO_3 and Li-deficient layer with more Ni(II). The former has been extensively investigated and confirmed the electrochemically inactive nature,[10,14,20–22] which will not only directly lead to the increase of the surface impedance, but also release CO/CO_2 during the first cycle, thereby partially break down the effective electrical contacts between the conductive additive and the active cathode materials.[27,28,55] In the latter, the presence of Ni(II) may also result in Li/Ni mixing,[9] and so degrading electrochemical activity. Although the induced surface reconstruction is unavoidable due to the intrinsic symmetry breaking of MO_6 polyhedral at the surface, it greatly depends on the chemical reactivity of the exposed atomic species. Accordingly, surface reconstruction can be suppressed by surface processing or coating, i.e., introducing chemically inactive cations, such as Al^{3+}, Ti^{4+}, Mn^{4+}, and La^{3+}.[46,59–64] In addition, design of core–shell and concentration gradient structured Ni-rich NMC, with Mn-rich surface, has been shown effective in stabilizing surface for long cycling stability.[65,66]

In this study, the strong dependence of surface reconstruction on the cooling rate, may open a new direction for suppressing surface reconstruction. As demonstrated in this study, quenching is one effective way, and may be combined with surface processing/coating to alleviate the issues associated with surface reconstruction for stabilizing the surface of the high-Ni layered oxide cathodes, for improved cycling stability and rate capability. Insights from this study on high Ni NMC, may also be applied to Li-rich layered oxides, and provide answers to some of the important questions, particularly regarding the impact of the cooling process on their structural ordering and electrochemical properties.[32–35]

In summary, high-performance $LiNi_{0.7}Mn_{0.15}Co_{0.15}O_2$ is obtained by quenching, exhibiting greatly improved rate capability compared to that via the general slow cooling process. Through in situ synchrotron X-ray study on the synthesis process coupled with surface analysis via various techniques (XPS, TXM-XANES, and TEM-EELS), cooling-induced surface reconstruction, including Li_2CO_3 accumulation, the formation of Li-deficient layer and Ni reduction at the particle surface, is uncovered to mainly occur at high temperatures (above 350 °C) due to the fast Li/O loss in the near-surface region, which is much different from, but has direct implications on the surface reconstruction during the storage or electrochemical cycling. The kinetics of surface reconstruction is cooling-rate dependent, and greatly suppressed by quenching, leading to an abrupt decrease of interfacial impedance and a significant increase of the rate capability. The findings will provide guidance to designing synthesis of high-Ni layered cathodes and, broadly, other materials of tailored surface properties.

Experimental Section

Synthesis of NMC71515: The hydroxide precursor for NMC71515, with nominal average composition of $Ni_{0.7}Mn_{0.15}Co_{0.15}(OH)_2$ was synthesized via a modified coprecipitation method. The precursor was completely mixed with LiOH in a molar ratio of 1:1.05 by grinding for 1 h. Then the mixture was loaded in a tube furnace to be heated to 500 °C by 5 °C min^{-1}, then held for 10 h to obtain the preheated mixture under O_2 flow. The preheated mixture was pressed into pellets for in situ experiments.

NMC71515 sample obtained by slow cooling was prepared by heating the preheated mixture at 850 °C for 5 h, then cooling it by 2 °C min^{-1} in the air. NMC71515 sample obtained by quenching was prepared by heating the preheated mixture at 850 °C for 5 h, then swiftly moving outside of the furnace for quenching in the air.

In Situ and Ex Situ High-Energy XRD Measurements: Time-resolved high-energy XRD patterns were collected from the preheated mixture mentioned above during calcination, at Sector 28–ID–2 of the

National Synchrotron Light Source II (NSLS-II) at Brookhaven National Laboratory. The wavelength of the X-ray beam was 0.18266 Å. For in situ experiments, the preheated mixture was pressed into pellets with the thickness around 1 mm and the diameter 7 mm, then placed in a furnace (Linkam TS 1500) vertically, with a window perpendicular to the X-ray beam. The pellets were then heated in air by following the temperature profile shown in the inset of Figure 3a. During the calcination, a 2D X-ray detector was deployed to collect the XRD patterns. The focused spot size is 0.5 mm (Horiz) × 0.5 mm (Vert).

Refinement of XRD Data: Rietveld refinements of selected XRD patterns were carried out using the General Structure Analysis Software (GSAS) package with the EXPGUI interface.[67,68] $LiCoO_2$ with the typical layered structure (space group $R\bar{3}m$) was employed as the initial structural model. The global refining parameters included background coefficients, peak shape parameters, lattice parameters, and the weights of different structures. For layered structure, the positional parameter of O (6c), the fractional factors of all Li, Ni, Co, and Mn, and isotropic atomic displacement parameters (U_{iso}) were refined. The chemical formula $(Li_{1-x}Ni_x)_{3b}(Ni_{0.7-x}Mn_{0.15}Co_{0.15}Li_x)_{3a}O_2$ was followed. That is, the total occupancy of Li and Ni at 3b sites and the total occupancy of Ni, Co, Mn, and Li at 3a sites were constrained to be unity; the atomic ratio of Ni: Mn: Co was constrained as stoichiometric, that is, 0.7:0.15:0.15. The U_{iso} of all elements sharing the same crystallography position was set to be equivalent.

Material Characterizations: A Zeiss SUPRA-55 scanning electron microscope (SEM) was used to record SEM images of the slow cooling and quenching samples. The weight loss for the slow cooling, quenching cases and Li_2CO_3 were tracked by a Mettler Toledo thermogravimetric analyzer, and the temperature profiles in the inset of Figure 3a were adopted to ensure the data consistency. XPS data were collected using an X-ray photoelectron spectrometer (Thermo Fisher). Inductively coupled plasma atomic emission spectroscopy (ICP-AES, JY2000-2, HORIBA JOBINYVON) was used to measure the precise elemental compositions (Li, Ni, Co, and Mn) of two ex situ samples.

Samples for TEM were prepared by dispersing the powder in ethanol and transferring it to a holey carbon-coated copper grid. HAADF images and EELS analyses were obtained using ARM 200CF (JEOL Ltd.). The microscope was equipped with a cold-field emission gun, double spherical aberration correctors (CEOS GmbH) and GIF Quantum (Gatan, Inc.) with dual EELS system. The microscopy was operated at 200 kV. EELS data were recorded in the scanning TEM (STEM) mode, with convergence and collection angles of 40 and 90 mrad, respectively. Background subtraction from the EELS spectra were processed using a power law fitting method.

TXM Measurements and Data Analysis: The hard X-ray chemical mapping were performed on full-field TXM at beamline 18-ID, NSLS-II. NMC71515 samples obtained by slow cooling and quenching were fixed in a custom-built holder mounted on a motorized X, Y, Z, and R stage. The X-ray beam could be focused on and transmitted through the region that was of interest by aligning the stages. The energy of the incident X-ray is scanned from 8200 to 8500 eV to cover whole Ni *K*-edge. The energy step is set as 1 eV in the range from 8320 to 8400 eV to improve the data quality and 10 eV in the other range to reduce the acquiring time. The Athena software is used to perform linear combination fitting for Ni *K*-edge XANES. The fitting range is set as −20 to 30 eV versus the absorption edge E0. Commercial NiO and $LiNiO_2$ are chosen as standards for Ni(II) and Ni(III), respectively.

Electrochemical Measurements: Ex situ samples obtained by slow cooling and quenching were used to perform the electrochemical measurements. Composite electrodes were prepared by blending 80 wt% of the active material, 10 wt% Super P as the conductive additive, and 10 wt% poly(vinylidenefluoride) (PVdF) as the binder in *N*-methyl-2-pyrrolidone. The slurry was blade-coated onto aluminum foil and dried at 100 °C for 12 h in a vacuum oven. Then electrode was cut into discs with diameter of 10 mm. Electrochemical tests were performed with CR2032 coin-type cells, which were assembled in an argon-filled glove box (VACCUM ATMOSPHERES Co.) with water and oxygen content below 0.5 ppm. The pure lithium foil was used as the anode. The glass microfiber filters (Whatman GF/D) was used as the separator. 1 M $LiPF_6$ solution in a mixture of EC, DEC, and DMC with a volume ratio of 1:1:1 was used as the electrolyte. The cells were charged and discharged in the galvanostatic mode at different rates (1 C = 200 mA h g^{-1}) using an ARBIN battery cycler in the voltage range of 3.0–4.3 V (vs Li^+/Li), all the above data were collected at 25 °C. Before the electrochemical measurement, the prepared cells were shelved for 1 h. The electrochemical impedance spectra were measured using a biological workstation in the frequency range of 0.1 Hz–1 MHz.

Supporting Information

Supporting Information is available from the Wiley Online Library or from the author.

Acknowledgements

This work was supported by the U.S. Department of Energy (DOE) Office of Energy Efficiency and Renewable Energy, Vehicle Technologies Office, Contract No. DE-SC0012704, the Guangdong innovative team program (2013N080), Guangdong Key-lab Project (No. 2017B0303010130), the peacock plan (KYPT20141016105435850), Shenzhen Science and Technology Research Grant (ZDSYS201707281026184), Chinese postdoctoral science foundation (2015M570882, 2015M570894). This research used 28-ID-2 (XPD) and 18-ID (FXI) beamlines at the National Synchrotron Light Source II, a U. S. DOE Office of Science User Facility operated for the DOE Office of Science by Brookhaven National Laboratory under Contract No. DE-SC0012704. The electron microscopy work at BNL is supported by the U.S. Department of Energy, Office of Basic Energy Science, Division of Materials Science and Engineering, under Contract No. DE-SC0012704. Research at the Argonne National Laboratory was funded by the US Department of Energy, Vehicle Technologies Office under contract no. DE-AC02-06CH11357.

Conflict of Interest

The authors declare no conflict of interest.

Keywords

high-Ni layered oxide cathodes, lithium-ion batteries, quenching, solid-state synthesis, surface reconstruction

Received: June 14, 2019
Revised: August 23, 2019
Published online: October 14, 2019

[1] J. B. Goodenough, K.-S. Park, *J. Am. Chem. Soc.* **2013**, *135*, 1167.
[2] M. S. Whittingham, *Chem. Rev.* **2014**, *114*, 11414.
[3] B. L. Ellis, K. T. Lee, L. F. Nazar, *Chem. Mater.* **2010**, *22*, 691.
[4] J. B. Goodenough, Y. Kim, *Chem. Mater.* **2010**, *22*, 587.
[5] C. Liu, F. Li, L. P. Ma, H. M. Cheng, *Adv. Mater.* **2010**, *22*, E28.
[6] B. Scrosati, J. Garche, *J. Power Sources* **2010**, *195*, 2419.
[7] M. D. Radin, S. Hy, M. Sina, C. Fang, H. Liu, J. Vinckeviciute, M. Zhang, M. S. Whittingham, Y. S. Meng, A. Van der Ven, *Adv. Energy Mater.* **2017**, *7*, 1602888.
[8] G. Assat, J.-M. Tarascon, *Nat. Energy* **2018**, *3*, 373.
[9] D. Wang, R. Kou, Y. Ren, C.-J. Sun, H. Zhao, M.-J. Zhang, Y. Li, A. Huq, J. Y. Peter Ko, F. Pan, Y.-K. Sun, Y. Yang, K. Amine, J. Bai, Z. Chen, F. Wang, *Adv. Mater.* **2017**, *29*, 201606715.

[10] Y. Li, R. Xu, Y. Ren, J. Lu, H. M. Wu, L. F. Wang, D. J. Miller, Y. K. Sun, K. Amine, Z. H. Chen, *Nano Energy* **2016**, *19*, 522.
[11] J. Q. Zhao, W. Zhang, A. Huq, S. T. Misture, B. L. Zhang, S. M. Guo, L. J. Wu, Y. M. Zhu, Z. H. Chen, K. Amine, F. Pan, J. M. Bai, F. Wang, *Adv. Energy Mater.* **2017**, *7*, 1601266.
[12] K. T. Lee, S. Jeong, J. Cho, *Acc. Chem. Res.* **2013**, *46*, 1161.
[13] P. Arora, R. E. White, M. Doyle, *J. Electrochem. Soc.* **1998**, *145*, 3647.
[14] S. T. Myung, F. Maglia, K. J. Park, C. S. Yoon, P. Lamp, S. J. Kim, Y. K. Sun, *ACS Energy Lett.* **2017**, *2*, 196.
[15] F. Lin, I. M. Markus, D. Nordlund, T. C. Weng, M. D. Asta, H. L. L. Xin, M. M. Doeff, *Nat. Commun.* **2014**, *5*, 3529.
[16] Y. D. Duan, L. Y. Yang, M. J. Zhang, Z. H. Chen, J. M. Bai, K. Amine, F. Pan, F. Wang, *J. Mater. Chem. A* **2019**, *7*, 513.
[17] J. Zheng, Y. Ye, T. Liu, Y. Xiao, C. Wang, F. Wang, F. Pan, *Acc. Chem. Res.* **2019**, *52*, 2201.
[18] H. S. Liu, Y. Yang, J. J. Zhang, *J. Power Sources* **2007**, *173*, 556.
[19] Y. Koyama, T. Mizoguchi, H. Ikeno, I. Tanaka, *J. Phys. Chem. B* **2005**, *109*, 10749.
[20] H. J. Noh, S. Youn, C. S. Yoon, Y. K. Sun, *J. Power Sources* **2013**, *233*, 121.
[21] C. H. Jo, D. H. Cho, H. J. Noh, H. Yashiro, Y. K. Sun, S. T. Myung, *Nano Res.* **2015**, *8*, 1464.
[22] J. Kim, Y. S. Hong, K. S. Ryu, M. G. Kim, J. Cho, *Electrochem. Solid-State Lett.* **2006**, *9*, A19.
[23] J. Sicklinger, M. Metzger, H. Beyer, D. Pritzl, H. A. Gasteiger, *J. Electrochem. Soc.* **2019**, *166*, A2322.
[24] A. M. Andersson, D. P. Abraham, R. Haasch, S. MacLaren, J. Liu, K. Amine, *J. Electrochem. Soc.* **2002**, *149*, A1358.
[25] G. V. Zhuang, G. Y. Chen, J. Shim, X. Y. Song, P. N. Ross, T. J. Richardson, *J. Power Sources* **2004**, *134*, 293.
[26] D. P. Abraham, R. D. Twesten, M. Balasubramanian, J. Kropf, D. Fischer, J. McBreen, I. Petrov, K. Amine, *J. Electrochem. Soc.* **2003**, *150*, A1450.
[27] D. J. Miller, C. Proff, J. G. Wen, D. P. Abraham, J. Bareno, *Adv. Energy Mater.* **2013**, *3*, 1098.
[28] S. E. Renfrew, B. D. McCloskey, *J. Am. Chem. Soc.* **2017**, *139*, 17853.
[29] D. H. Cho, C. H. Jo, W. Cho, Y. J. Kim, H. Yashiro, Y. K. Sun, S. T. Myung, *J. Electrochem. Soc.* **2014**, *161*, A920.
[30] X. H. Xiong, Z. X. Wang, P. Yue, H. J. Guo, F. X. Wu, J. X. Wang, X. H. Li, *J. Power Sources* **2013**, *222*, 318.
[31] K. Park, J. H. Park, B. Choi, J. H. Kim, S. G. Hong, H. N. Han, *Electrochim. Acta* **2017**, *257*, 217.
[32] E. McCalla, A. W. Rowe, C. R. Brown, L. R. P. Hacquebard, J. R. Dahn, *J. Electrochem. Soc.* **2013**, *160*, A1134.
[33] E. McCalla, C. M. Lowartz, C. R. Brown, J. R. Dahn, *Chem. Mater.* **2013**, *25*, 912.
[34] B. R. Long, J. R. Croy, F. Dogan, M. R. Suchomel, B. Key, J. G. Wen, D. J. Miller, M. M. Thackeray, M. Balasubramanian, *Chem. Mater.* **2014**, *26*, 3565.
[35] F. S. Feng, H. S. Fang, B. Yang, W. H. Ma, Y. B. Dai, *Int. J. Electrochem. Sci.* **2014**, *9*, 6852.
[36] K. Heo, J. S. Lee, H. S. Kim, J. Kim, J. Lim, *J. Electrochem. Soc.* **2017**, *164*, A2398.
[37] M. C. Biesinger, B. P. Payne, A. P. Grosvenor, L. W. M. Lau, A. R. Gerson, R. S. Smart, *Appl. Surf. Sci.* **2011**, *257*, 2717.
[38] F. Wu, J. Tian, Y. F. Su, J. Wang, C. Z. Zhang, L. Y. Bao, T. He, J. H. Li, S. Chen, *ACS Appl. Mater. Interfaces* **2015**, *7*, 7702.
[39] M. Y. Ge, D. S. Coburn, E. Nazaretski, W. H. Xu, K. Gofron, H. J. Xu, Z. J. Yin, W. K. Lee, *Appl. Phys. Lett.* **2018**, *113*, 083109.
[40] D. S. Coburn, E. Nazaretski, W. Xu, M. Ge, C. Longo, H. Xu, K. Gofron, Z. Yin, H. H. Chen, Y. Hwu, W.-K. Lee, *Rev. Sci. Instrum.* **2019**, *90*, 053701.
[41] S. Muto, Y. Sasano, K. Tatsumi, T. Sasaki, K. Horibuchi, Y. Takeuchi, Y. Ukyo, *J. Electrochem. Soc.* **2009**, *156*, A371.
[42] S. Hwang, E. Jo, K. Y. Chung, K. S. Hwang, S. M. Kim, W. Chang, *J. Phys. Chem. Lett.* **2017**, *8*, 5758.
[43] S. J. Zheng, R. Huang, Y. Makimura, Y. Ukyo, C. A. J. Fisher, T. Hirayama, Y. Ikuhara, *J. Electrochem. Soc.* **2011**, *158*, A357.
[44] Y. J. Bi, T. Wang, M. Liu, R. Du, W. C. Yang, Z. X. Liu, Z. Peng, Y. Liu, D. Y. Wang, X. L. Sun, *RSC Adv.* **2016**, *6*, 19233.
[45] I. A. Shkrob, J. A. Gilbert, P. J. Phillips, R. Klie, R. T. Haasch, J. Bareno, D. P. Abraham, *J. Electrochem. Soc.* **2017**, *164*, A1489.
[46] Y. You, H. Celio, J. Li, A. Dolocan, A. Manthiram, *Angew. Chem., Int. Ed.* **2018**, *57*, 1.
[47] X. B. Zheng, X. H. Li, Z. X. Wang, H. J. Guo, Z. J. Huang, G. C. Yan, D. Wang, *Electrochim. Acta* **2016**, *191*, 832.
[48] H. S. Liu, Y. Yang, J. J. Zhang, *J. Power Sources* **2006**, *162*, 644.
[49] A. R. Armstrong, M. Holzapfel, P. Novak, C. S. Johnson, S. H. Kang, M. M. Thackeray, P. G. Bruce, *J. Am. Chem. Soc.* **2006**, *128*, 8694.
[50] A. Jarry, S. Gottis, Y. S. Yu, J. Roque-Rosell, C. Kim, J. Cabana, J. Kerr, R. Kostecki, *J. Am. Chem. Soc.* **2015**, *137*, 3533.
[51] A. Banerjee, Y. Shilina, B. Ziv, J. M. Ziegelbauer, S. Luski, D. Aurbach, I. C. Halalay, *J. Am. Chem. Soc.* **2017**, *139*, 1738.
[52] H. H. Zheng, Q. N. Sun, G. Liu, X. Y. Song, V. S. Battaglia, *J. Power Sources* **2012**, *207*, 134.
[53] J. Eom, M. G. Kim, J. Cho, *J. Electrochem. Soc.* **2008**, *155*, A239.
[54] K. Shizuka, C. Kiyohara, K. Shima, Y. Takeda, *J. Power Sources* **2007**, *166*, 233.
[55] H. S. Liu, Z. R. Zhang, Z. L. Gong, Y. Yang, *Electrochem. Solid-State Lett.* **2004**, *7*, A190.
[56] N. Mijung, Y. Lee, J. Cho, *J. Electrochem. Soc.* **2006**, *153*, A935.
[57] O. Haik, N. Leifer, Z. Samuk-Fromovich, E. Zinigrad, B. Markovsky, L. Larush, Y. Goffer, G. Goobes, D. Aurbach, *J. Electrochem. Soc.* **2010**, *157*, A1099.
[58] R. Jung, R. Morasch, P. Karayaylali, K. Phillips, F. Maglia, C. Stinner, Y. Shao-Horn, H. A. Gasteiger, *J. Electrochem. Soc.* **2018**, *165*, A132.
[59] A. M. Wise, C. M. Ban, J. N. Weker, S. Misra, A. S. Cavanagh, Z. C. Wu, Z. Li, M. S. Whittingham, K. Xu, S. M. George, M. F. Toney, *Chem. Mater.* **2015**, *27*, 6146.
[60] Y. S. Lee, W. K. Shin, A. G. Kannan, S. M. Koo, D. W. Kim, *ACS Appl. Mater. Interfaces* **2015**, *7*, 13944.
[61] Y. P. Chen, Y. Zhang, B. J. Chen, Z. Y. Wang, C. Lu, *J. Power Sources* **2014**, *256*, 20.
[62] K. C. Kam, M. M. Doeff, *J. Mater. Chem.* **2011**, *21*, 9991.
[63] Z. C. Liu, H. H. Zhen, Y. Kim, C. D. Liang, *J. Power Sources* **2011**, *196*, 10201.
[64] H. P. Yang, H. H. Wu, M. Y. Ge, L. J. Li, Y. F. Yuan, Q. Yao, J. Chen, L. F. Xia, J. M. Zheng, Z. Y. Chen, J. Duan, K. Kisslinger, X. C. Zeng, W. K. Lee, Q. B. Zhang, J. Lu, *Adv. Funct. Mater.* **2019**, *29*, 1808825.
[65] Y. K. Sun, S. T. Myung, B. C. Park, J. Prakash, I. Belharouak, K. Amine, *Nat. Mater.* **2009**, *8*, 320.
[66] Y. K. Sun, Z. H. Chen, H. J. Noh, D. J. Lee, H. G. Jung, Y. Ren, S. Wang, C. S. Yoon, S. T. Myung, K. Amine, *Nat. Mater.* **2012**, *11*, 942.
[67] B. H. Toby, *J. Appl. Crystallogr.* **2001**, *34*, 210.
[68] A. C. Larson, R. B. V. Dreele, *General Structure Analysis System (GSAS), LAUR 86–748*, Los Alamos National Laboratory, Los Alamos, NM **2000**.